To be published in IEEE Aerospace Conference Proceedings, **2003**, Cat No. 0-7803-7651-X/03/$17.00 © 2003 IEEE

Planar REDOX and Conductivity Sensors for ISS Water Quality Measurements[1]

Martin G. Buehler, Gregory M. Kuhlman, Didier Keymeulen, and Nosang V. Myung
Jet Propulsion Laboratory, California Institute of Technology
and
Samuel P. Kounaves, Department of Chemistry. Tufts University

Abstract—- Bare-metal based REDOX and conductivity sensors that are used to detect ionic species in solution by measuring the electrochemical cell current as the voltage is scanned. The simplicity and robustness of these sensors allows their use in the analysis of ionic species found in natural and drinking water. The measurements include 1) conductivity measurements which provide a gross indication of the ion concentrations present in solution, 2) Cyclic Voltammetry (CV) which provide a survey of electroactive species, and 3) Anodic Stripping Voltammetry (ASV) which allow ion identification and quantification. The ions detected are Zn, Fe, Pb, Cu, and Ag and the methodology for their extraction is discussed. Also discussed is the dependence of ASV results on the deposition time and voltage scan rate. This paper also describes the construction of the sensors, the potentiostat electronics, the measurement methodology, and applications to water quality measurements.

TABLE OF CONTENTS

1. INTRODUCTION

This paper extends the work reported at last year's IEEE Aerospace conference where the design principles and fabrication of Electronic Tongue No. 1 (E-Tongue 1) were described [1]. The E-Tongue 2 substrate contains a number of sensors but only the characterization of the REDOX electrodes and conductivity sensors are described in this paper. REDOX sensors were characterized using Cyclic Voltammetry (CV) [2] and Anodic Stripping Voltammetry (ASV) [3]. The additional sensors are ISEs (Ion Selective Electrodes) and GAL (Galvanic) Arrays composed of dissimilar metals such as Ni, Fe, Cu, and Zn and are intended for metal corrosion studies. The substrate also contains a thermometer and heater. The blue dots are dielectric material covering 39 pins used to connect the sensors via underside traces to the electronics board to be discussed later.

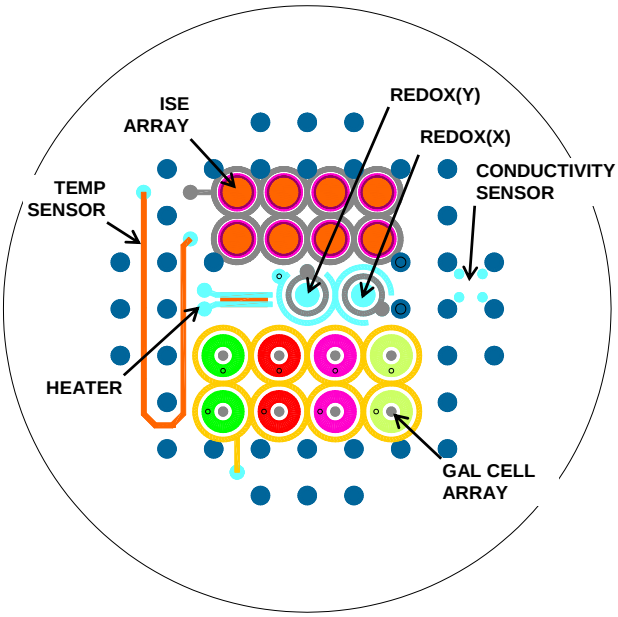

Figure 1. Schematic view of E-Tongue 2 3.3-cm (1.3-inch) diameter ceramic substrate with 20 sensors and one heater.

This effort is an outgrowth of the 25-cm^3 electrochemical cell developed for the MECA (Mars Environmental Compatibility Assessment) project [4] which included 20 prefabricated Ion Selective Electrodes (ISE), a conductivity sensor, a temperature sensor and an REDOX potential sensor. Commercial electrochemical sensors are typically fabricated at the end of a pencil-like cylindrical tube. Such sensors cannot be configured easily in a multi-sensor array nor can they be miniaturized.

The goal of this effort is to develop long-life electrochemical sensors for water quality measurements for use on the International Space Station (ISS) Alpha and Martian habitats. A list of the trace elements found in drinking water and the allowable contamination limits is given in Table 1. The allowable contamination limits are

[1] 0-7803-7651-X/03/$17.00 © 2003 IEEE

given in mg/L and µM [5] along with reduction potentials, E° [6].

Table 1. Drinking Water Trace Contaminates

Name	Com-pound	Molecular Weight g/mol	ppm= mg/L [5]	µM	E° V [6]
Ammonia	NH4+	17.03	0.5	29.360	-0.762
Arsenic	As	75.9216	0.01	0.132	-0.608
Barium	Ba	137.33	1	7.282	-2.912
Cadmium	Cd	112.41	0.05	0.445	-0.403
Calcium	Ca	40.08	30	748.503	-3.8
Chloride	Cl	35.45	200	5641.749	1.358
Chromium	Cr	51.996	0.05	0.962	-0.913
Copper	Cu	63.54	1	15.738	0.153
Iodine	I2	253	15	59.289	0.5355
Iron	Fe	55.85	0.3	5.372	-0.447
Lead	Pb	207.2	0.05	0.241	-0.126
Magnesium	Mg	24.3	50	2057.613	-2.372
Manganese	Mn	24.32	0.05	2.056	-1.185
Mercury	Hg	200.59	0.002	0.010	0.851
Nickel	Ni	58.69	0.05	0.852	-0.257
Nitrate	NO3-	62	10	161.290	?
Potassium	K	30.1	340	11295.681	-2.931
Selenium	Se	78.96	0.01	0.127	-0.924
Silver	Ag	107.868	0.05	0.464	-0.8
Sulfate	SO4	96.07	250	2602.269	0.172
Zinc	Zn	65.38	5	76.476	-0.762

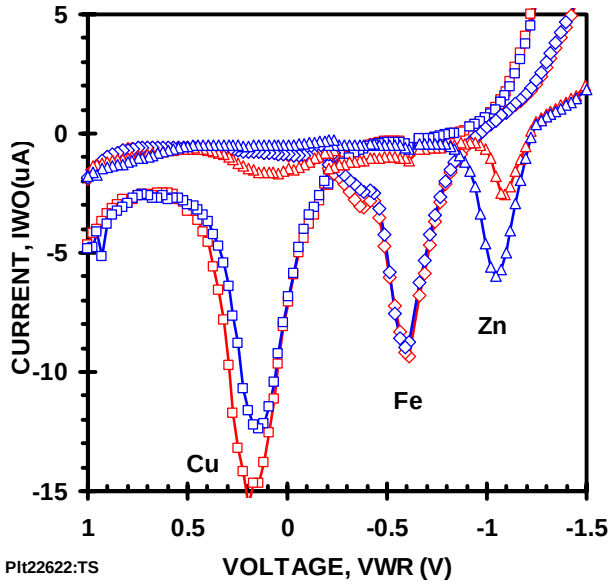

Figure 2. ASV data for three heavy metal ions with 1 mM concentration. The scan rate was 100 mV/s, Tdep = 5 s for $CuSO_4$, Tdep = 100 s for $FeSO_4$, and Tdep = 100 s for $ZnSO_4$.

The measurements in this paper represent a start at developing the methodology that will be directed toward detecting the target ions such as K^+ (340 mg/L), Ca^{2+} (30 mg/L), Mg^{2+} (50 mg/L) and Cl^- (200 mg/L) which represent some of the NASA Spacecraft Maximum Contaminant Levels (MCL) for potable water for International Space Station Alpha.

Typical results obtained from the REDOX sensor is shown in Fig. 2. Here the sensor was sequentially exposed to 1 mM $CuSO_4$, $FeSO_4$, and $ZnSO_4$. The data were acquired using ASV, (Anodic Stripping Voltammetry) at the stated deposition time, Tdep and scan rate, S. In the figure two curves are shown for each ion to delineate repeatability issues. The red curve was taken first followed by the blue trace. For the data shown in Fig. 2, a negative potential of -1.5 V was applied to the working electrode, WE, for a deposition time, Tdep. The voltage was then scanned to +1 V. The ions re-enter the solution (oxidized) at a redox potential related to the ion's position in the Electrochemical Series. Thus, the *possible* chemical identity of an unknown ion can be tentatively bounded by this technique. The uncertainty in the identification is do to lack of uniqueness of the redox potential since there are a number of ions or molecules that can have the same potential.

2. E-TONGUE SENSORS

A photograph of the substrate used in this experiment is shown in Fig. 3.

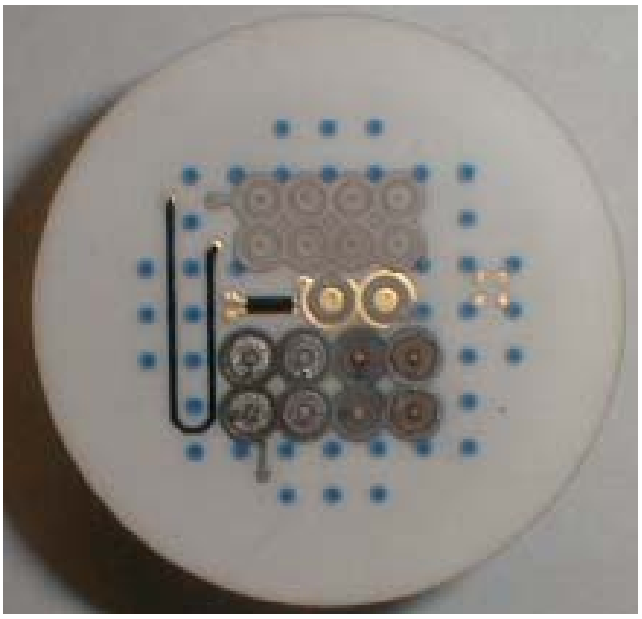

Figure 3. E-Tongue 2 3.3-cm (1.3-inch) diameter ceramic substrate; see Fig. 1 for sensor identification.

The ceramic substrate contains eight ISE (Ion Selective Electrodes), eight galvanic cells, two REDOX electrodes, one conductivity sensors, one thermometer and one heater. Only the REDOX and conductivity sensors are discussed in this paper. REDOX(X) and REDOX(Y) are identified in Fig. 1.

The substrate was fabricated using hybrid microelectronic fabrication methods where each layer is screen printed onto the ceramic substrate and fired in an air atmosphere at 900°C. The substrate is 1-mm thick and is 96% alumina. Electrical contact to the sensors is achieved using 0.25-mm laser drilled vias. The vias are made conducting by screen printing a layer that is drawn through the vias using a mild vacuum which is followed by a firing cycle. The vias are connected to wires that are screen printed on the underside of the substrate and connected to pins. The location of the pins is visible on the substrate shown in Figs. 1 and 3 as blue dots which are screen-printed dielectrics used to seal the pin head from exposure to the electrolyte that eventually covers the sensors. The substrate contains 39 electrical contacts (pins).

Photomicrographs of the REDOX electrodes are shown in Figs. 4a and 4b. The inner electrode is a Au(12)Pt(88) working electrode, WE, the inner ring is a Pd(12)Ag(88) reference electrode, RE, and the outer ring is a Au(12)Pt(88) auxiliary electrode, AE. The WE is 1.25 mm in diameter, the RE is 0.25 mm wide and separated from the other electrodes by 0.25 mm, and the inner diameter of the AE is 2.75-mm.

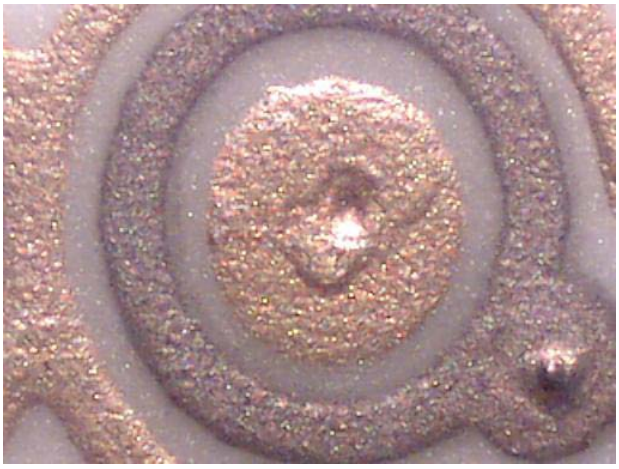

Figure 4a. Photomicrograph of REDOX(X) sensor. The diameter of the WE, center dot, is 0.75 mm.

In operation the REDOX electrode is biased so ions flow between the WE and the AE in a three-dimensional circular pattern. The RE is used to sense the potential between the WE and AE. Thus, the measured potential consists of the potential drop across the double layer at the WE and the series resistance (IR loss) of the electrolyte between the WE and RE. This is a unique planar design where the RE surrounds the WE and the AE surrounds the RE. Because the AE is grounded, this allows the AE to be shared with other sensors and it isolates the structures from interfering with each other. Concentric circular ultramicroelectrodes [7] have been fabricated but did not consider using a common, grounded AE with individually addressable RE and WE's.

The Pd(12)Ag(18) RE electrodes turned out to be a problem in that the silver readily forms dendrites in solution. These dendrites grow and short to adjacent electrodes. Pd(12)Ag(18) electrodes were chloridize to minimize dendrite growth. However, they were unsuccessful. In future versions, the RE electrodes will be fabricated using different materials.

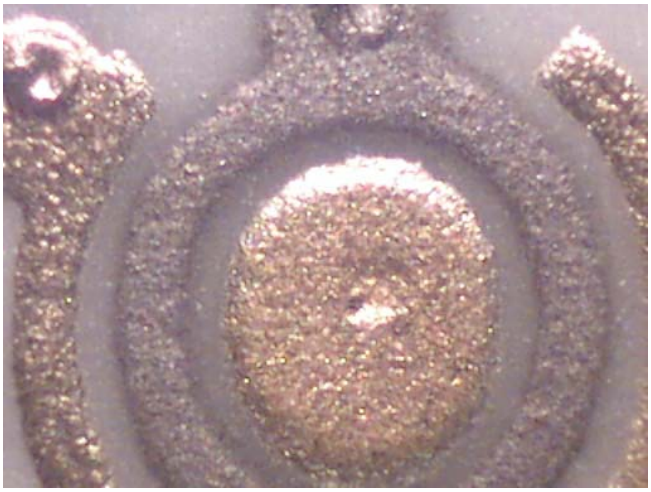

Figure 4b. Photomicrograph of REDOX(Y) sensor

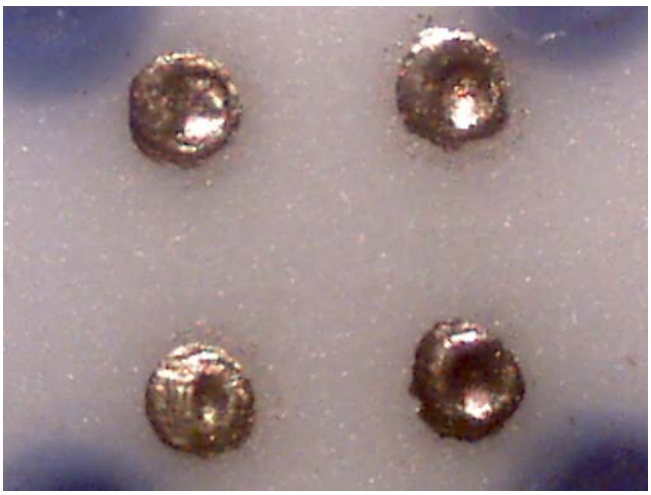

Figure 5. Photomicrograph of the conductivity sensor where the electrode spacing is 1.25 mm.

A photomicrograph of the conductivity sensor is seen in Fig. 5. It consists of four Au(12)Pt(88) electrodes (0.5 mm in diameter) and are separated by 1.25 mm

3. APPARATUS

The electronics used to measure the REDOX and conductivity sensors is shown in Figs. 6 and 7, respectively. The REDOX circuitry shown in Fig. 6 is a dual potentiostat. That is, each REDOX electrode has its own potentiostat that is driven from a common DAC (Digital-to-Analog-Converter). The current through the two REDOX electrodes is measured independently. In practice it was found that the current and voltages through both devices were most often within a few percent of each other.

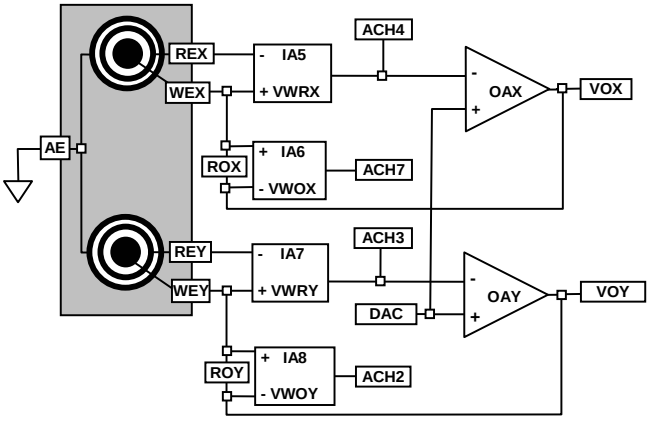

Figure 6. Dual potentiostat circuitry for two REDOX electrodes.

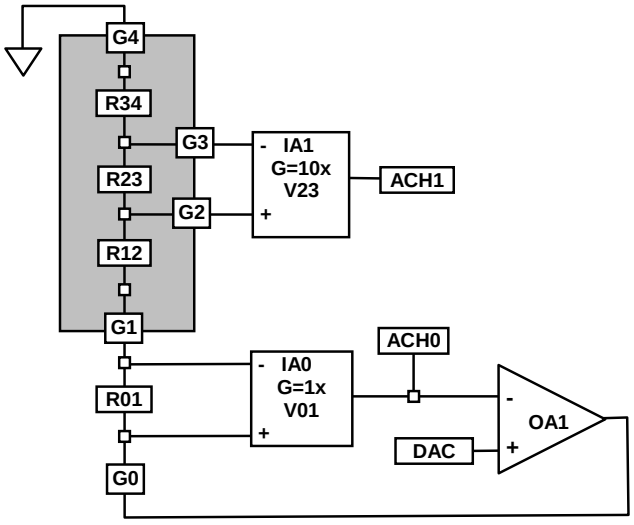

Figure 7. Galvanostat circuitry for the conductivity sensor.

The key feature of this design is the shared AE that is in common with both sensors. This feature reduces the number of pins or wires from the sensor pair and reduces the wire count when the sensors are connected in large arrays. In addition, the AE is grounded and this provides an intrinsic isolation of each sensor in that their electric fields do not interfere. Another advantage of a grounded AE is that it provides a ground plane for the entire cell that acts like an electrical shield that reduces noise. The common, grounded AE is a unique feature of this REDOX sensor design.

In operation, the output of the IA (Instrumentation Amplifier) connected between WE and RE is presented to the OA (Operational Amplifier). Using feedback, the OA forces a current through the REDOX electrode until the output of the IA (IA5, for example) and the DAC are equal.

Circuitry used in measuring the conductivity sensor is shown in Fig. 7. It is configured as a galvanostat and is used to force a current through adjacent electrodes found in the conductivity sensor seen in Fig. 5. The voltage drop is measured between the other two electrodes.

An overview of the apparatus used in these experiments is shown in Fig. 8. It consists of the ceramic substrate mounted in a Delrin® chamber. Several types of chambers were constructed including a flow-through (~1-mL capacity) and open top chamber (~5-mL capacity). In this figure, an open top chamber is displayed and mounted in a ZIF (Zero-Insertion-Force) socket that is mounted on a printed circuit board containing the circuitry. Using one of the connectors seen on the left of the board, the board is connected to a data acquisition card (NI-DAQ-1200) that contains a 12-bit ADC (Analog-to-Digital-Converter) and a 12-bit DAC. The instrument is programmed in Visual Basic.

Figure 8. E-Tongue 2 electronics apparatus fabricated on a 10-cm by 15 cm printed circuit board.

The chamber has a double O-ring design where the O-rings are positioned on the top and bottom of the ceramic and clamped into place using the six screws visible on the top of the chamber. This provides for a water-tight seal that does not place a bending stress on the ceramic substrate.

The ceramic will crack if subjected to a bending moment. In operation, the chamber is first sonicated in water for 10 minutes. The ceramic substrate was mechanically scrubbed and rinsed with water to remove surface deposits. The electrolyte is introduced into the chamber. During some measurements, the chamber is covered with tape to prevent aeration of the electrolyte.

4. WAVEFORMS

In the measurements, three waveforms including Triangle Step Wave, Ramp Step Wave, and Ramp Square Wave were used where each waveform is associated with a particular measurement method. A triangular step wave is used with the CV (Cyclic Voltammetry) method. Two waveforms are used for the ASV, a single linear ramped step wave and a ramped square wave (SWASV). The SWASV is currently under development and will be presented when its analysis is more fully developed. The second derivative of the ASV response was calculated as explained below; this is termed D2ASV

The wave shapes used in these measurements are shown in Fig. 9 where E1 is a positive voltage and E2 is a negative voltage. The waves were created using a 12-bit DAC with a resolution of 2.5 mV. A total of 100 data points were taken between E1 and E2. For a span (E1 – E2) of 2 V, each step was 20 mV. The measurements were conducted at a stated scan rate, S, and seven Tdep times which varied from 10 s to 1000 s in a 1, 2, 5 sequence. The overall measurement time was approximately 4 hours.

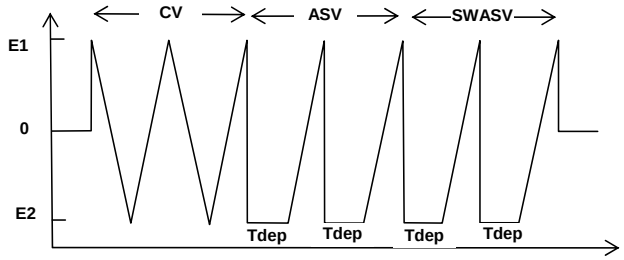

Figure. 9. Overview of the waveforms for the three measurement methods used in REDOX electrodes.

5. CONDUCTIVITY MEASUREMENTS

The conductivity measurements utilized the circuitry shown in Fig. 7. Since conductivity can not be measured reliably using dc [2], a current-ramp triangle wave was used. A time varying current is required because the conducting carriers in solution are ions, not electrons. For conduction to occur, ions must continually exchange electrons with an electrode through electrochemical oxidation or reduction reaction and this requires a time varying signal.

The circuitry shown in Fig. 2 is a galvanostat where current is forced through the conductivity cell and the voltage across the potential probes, V23, is measured. The current is generated by the DAC. The current is the DAC voltage divided by the resistor, R01. The resistance of the cell is V23*R01/V01. With a DAC sweep rate of 1 V/s, the current ramp is 10 µA/s. Figure 10 shows the I-V characteristic of conductivity sensor for different HCl concentrations listed in the legend of Fig. 10. As seen in the figure, the zero-current intercept voltage is different for each electrolyte. This behavior, is the motivation for using a galvanostat circuit instead of a potentiostat.

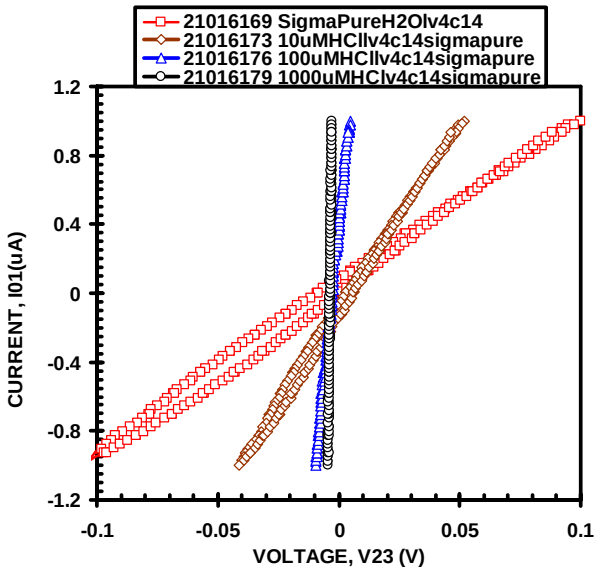

Fig. 10 Conductivity sensor response to pure water and three HCl solutions.

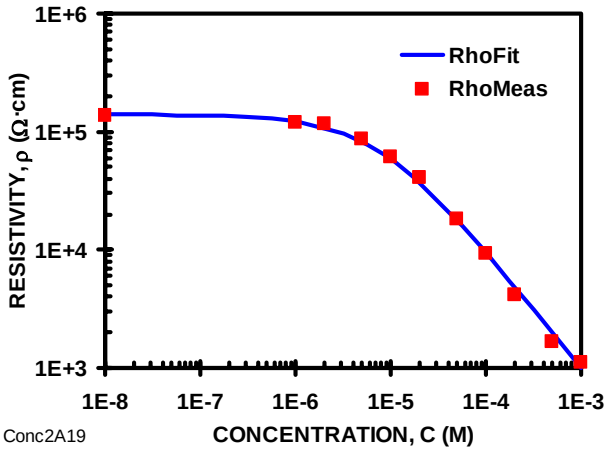

Figure 11. Conductivity sensor HCl response.

It is essential to turn the conductivity sensor off when not in use by specifying zero current. Forcing zero-current puts the sensor in an electrochemically inactive state. An

alternate approach is to drive the sensor with a potentiostat where the turn-off state is zero volts. As seen in Fig. 10, at zero volts significant current flows and this can cause deposition of an electroactive species on the driven electrodes of the conductivity sensor.

The solution resistance, R, was determined from the slope of the data seen in Fig. 10 using a least squares fitting technique. The solution resistivity, ρ, for the four-probe seen in Fig. 5 is assumed [8] to follow:

$$\rho = G_f \cdot d \cdot R \qquad (1)$$

where d = 0.125 cm is the distance between adjacent probes seen in Fig. 5 and the geometrical factor is G_f = 10.726. The results are shown as measured data points, RhoMeas, in Fig. 11.

A simple model was developed to fit the results seen in Fig. 11. Two resistors are placed in parallel. One resistor represents the as-received water resistance, R_0, and the other resistor represents the electrolyte resistance, R_e. The total resistance, R, is:

$$R = \frac{R_0}{\left(1 + \frac{R_0}{R_e}\right)} \qquad (2)$$

The water resistance is given by:

$$R_0 = \rho_0/(10.726 \cdot d) \qquad (3)$$

The electrolyte resistance was formulated from a combination of Eq. 1 subscripted for the electrolyte and the definition of the electrolyte resistivity [2]:

$$\rho_e = 1000/(\lambda_e \cdot C_e) \qquad (4)$$

where λ_e is the electrolyte's equivalent ionic conductivity. The combination of the above equations yields:

$$R_e(\Omega) = \frac{1000}{10.726 \cdot d(cm) \cdot \lambda_e \left(\frac{cm^2}{\Omega \cdot mol}\right) \cdot C_e(M)} \qquad (5)$$

Substituting Eqs. 1, 3 and 5 into Eq. 2 yields the fitting equation:

$$\rho = \frac{\rho_0}{1 + \left(\frac{\rho_0 \cdot \lambda_e}{1000}\right) C_e} \qquad (6)$$

The result of the curve fitting process yields ρ_0 = 140 kΩ-cm and λ_e = 988 $cm^2/(\Omega \cdot mol)$. The resistivity of clean water should be near 18 MΩ-cm so the low value for ρ_0 indicates that the water contains residual contaminates. For HCl, the value for λ_e is 421 $cm^2/(\Omega \cdot mol)$ at 1 mM [6]. Both extracted values are sensitive to the $G_f \cdot d$ product. Future investigations are directed at determining a suitable value for the $G_f \cdot d$ product to allow quantatative measurements.

6. CV MEASUREMENTS

The CV method provides a survey of the electroactive species in solution. An example is seen in Fig. 12 for as-received water. In our methodology, this curve is acquired seven times, once after each Tdep cycle. In principle the set of curves should be independent of the Tdep and so provides insight into the stability of the solution over the four-hour measurement cycle.

The wave shape, shown in Fig. 12, is unique to the E-Tongue 2 electrodes where all three electrodes are planar. The peaks that appear at -0.1 and -0.75 V grow with Tdep. The origin of this feature has recently been identified as electrolysis (bubbles) generated at the heater and thermometer electrodes seen in Fig.1. The lesson learned is similar to the conductivity sensor lesson learned. That is, all devices except the one under test must be turned off and that requires zero current flow through the off device not zero voltage. The feature that appears at -0.75 V is also seen in the following data but seems to provide only a baseline shift.

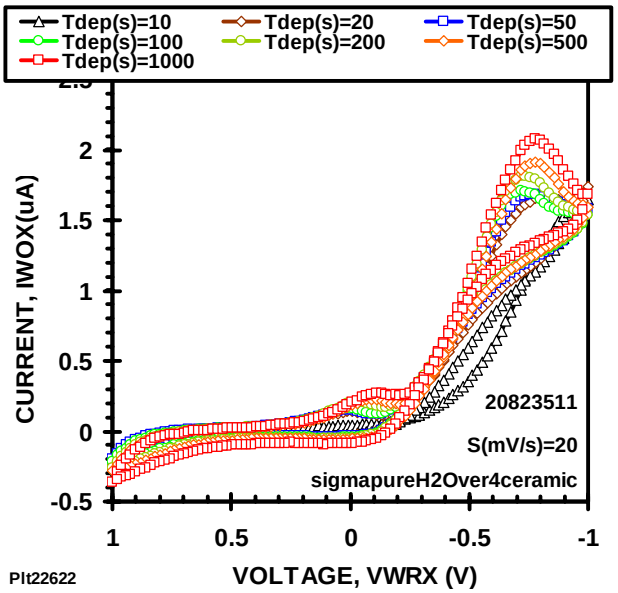

Figure 12. CV response for Sigmapure water

7. ASV MEASUREMENT CONDITIONS

The ASV technique provides for concentrating reduceable ions at the WE; thus, this technique can have sensitivities in the pM (pico-molar) range [3]. The operating conditions for the ASV method are well described by the data shown in Fig. 13.

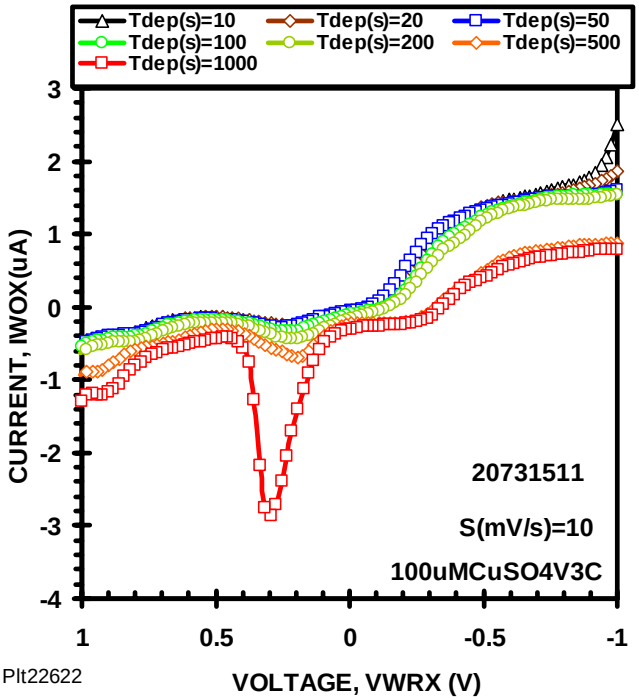

Figure 13a. ASV response for 100 µM $CuSO_4$ scanned at 10 mV/s.

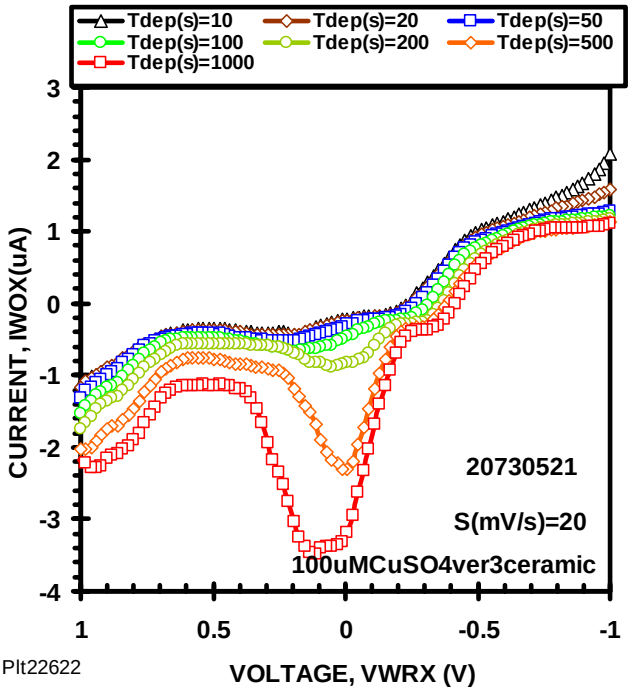

Figure 13b. ASV response for 100 µM $CuSO_4$ scanned at 20 mV/s.

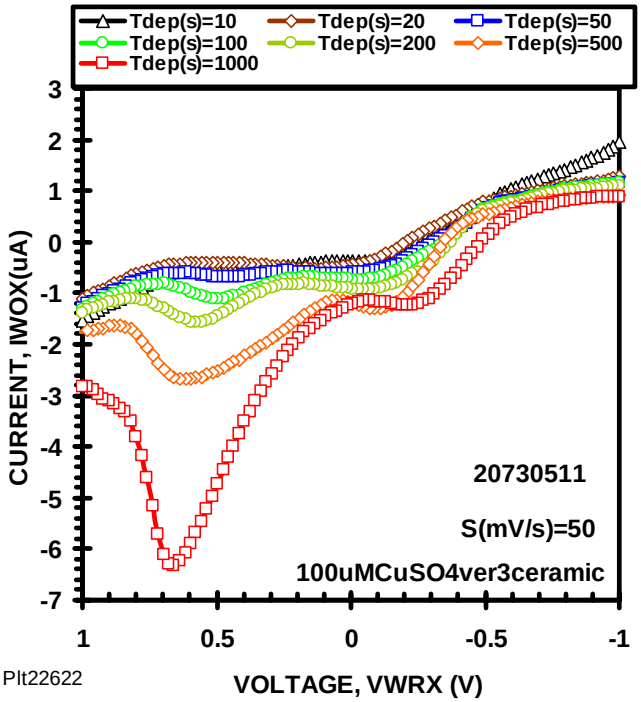

Figure 13c. ASV response for 100 µM $CuSO_4$ scanned at 50 mV/s.

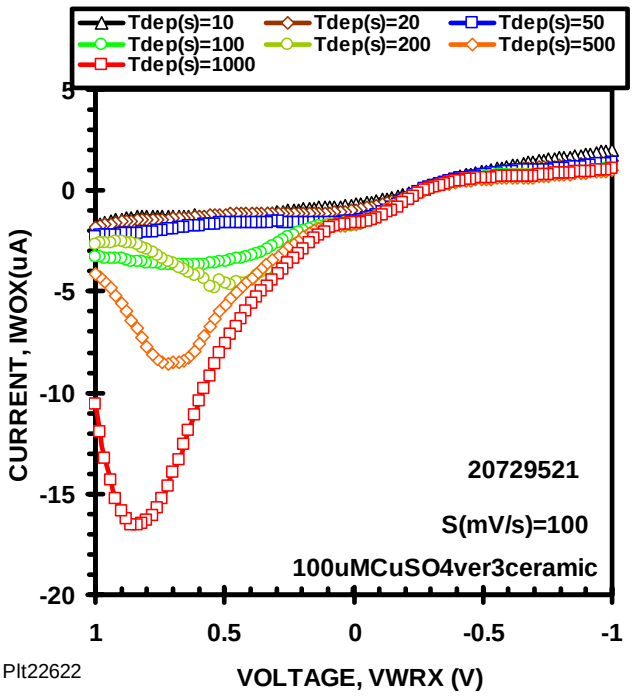

Figure 13d. ASV response for 100 µM $CuSO_4$ scanned at 100 mV/s.

The data in Fig. 13 was was acquired using 100 µM $CuSO_4$ and was scanned at four dfferent rates and seven deposition times. The ASV method begins with a deposition time, Tdep. Referring to the voltage waveform as shown in Fig. 9, the voltage is scanned from a negative voltage, E2, to a positive voltage, E1, at a linear scan rate of S.

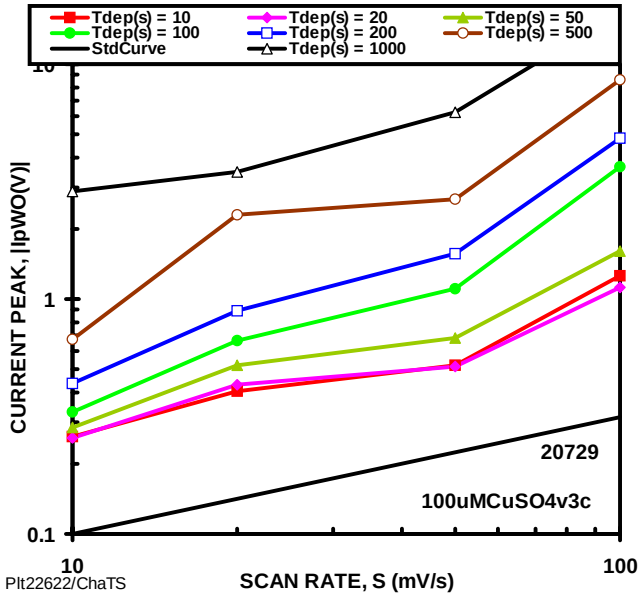

Figure 14a. Analysis of the data seen in Fig. 13 showing that current peak is a function of the square root of the scan rate.

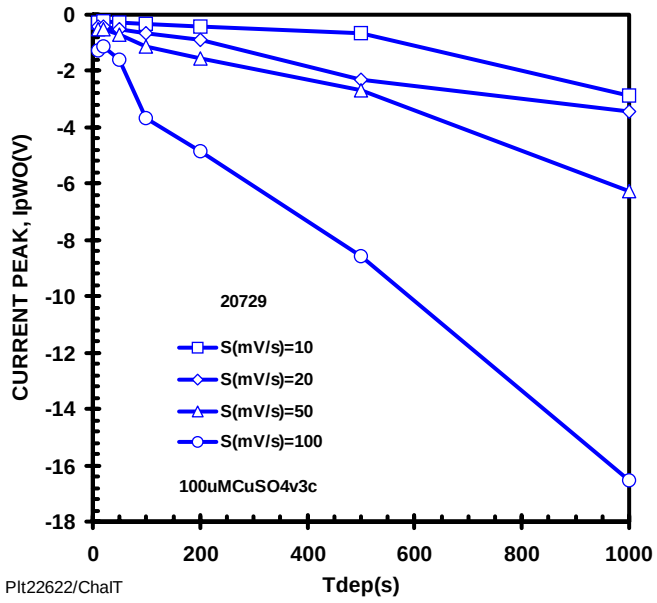

Figure 14b. Analysis of the data seen in Fig. 13 showing the linear dependence of the current peak on deposition time.

The process is repeated twice in order to observe the stability of the measurement. In most cases the second trace overlapped the first trace. Except for the data in Fig. 2, the results reported in this study are for the second trace and for the REDOX(X) device. The peak currents are plotted Fig. 14a as a function of scan rate and in Fig. 14b as a function of deposition time.

The effect of the scan rate on the current peak height, IpWO, is seen in Fig. 14a. The data generally have a slope of 0.5 on this log-log plot. The behavior of the slope and the fact that the voltage peak is scan rate dependent as seen in Fig. 13 leads to the choice of the of a totally irreversible system [9]. The peak current is:

$$Ip = 2.99 \cdot 10^5 \cdot \alpha^{1/2} \cdot A \cdot D^{1/2} \cdot C \cdot S^{1/2} \qquad (7)$$

where α is the transfer coefficient, A the area of the WE, D the diffusion coefficient, C the concentration of the electroactive species, and S the scan rate. The data in Fig. 14b indicates that the deposition time, Tdep, is proportional to concentration. This behavior on concentration is also described by Eq. 7.

Operating principles for ASV measurements are summarized as follows:

1. Larger peak currents occur at higher Tdep and scan rate. This is an important consideration when attempting to measure trace ionic species.

2. The penalty for operating at higher Tdep and S values is that the peak voltage shifts toward more positive voltages. At higher S values, the ASV base-line slope also increases due charging of the double-layer capacitance.

8. ASV EXPERIMENTS

The value of the ASV technique is found in its ability to detect low-concentrations of ionic species in solution, to provide probable identities for the electroactive species from their redox potentials, and to quantify the concentration of species. In this study, the focus is on determining the redox potential by extraploating peak current-voltage values to zero peak current.

ASV results were obtained from four solutions containing $PbCl_2$ (Fig. 15), $ZnSO_4$ (Fig. 16), $CuSO_4$ (Fig. 17), and NaCl (Fig. 18). In these figures, the ASV results are presented, then the calculated second derivative curves, followed by the peak current-voltage curves.

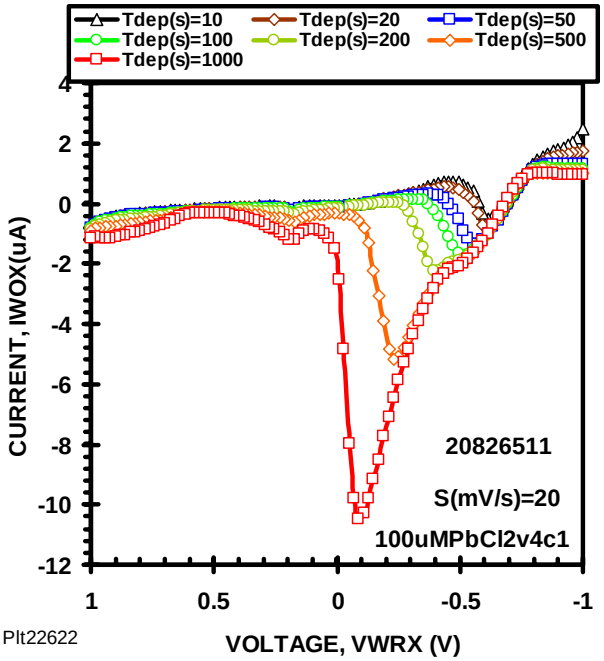

Figure 15a. ASV response for 100 µM $PbCl_2$

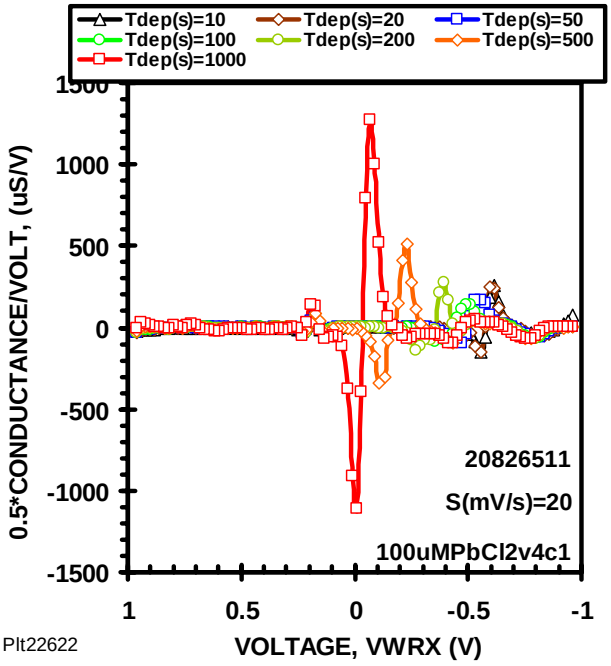

Figure 15b. D2ASV response for 100 µM $PbCl_2$ data seen in Fig. 15a.

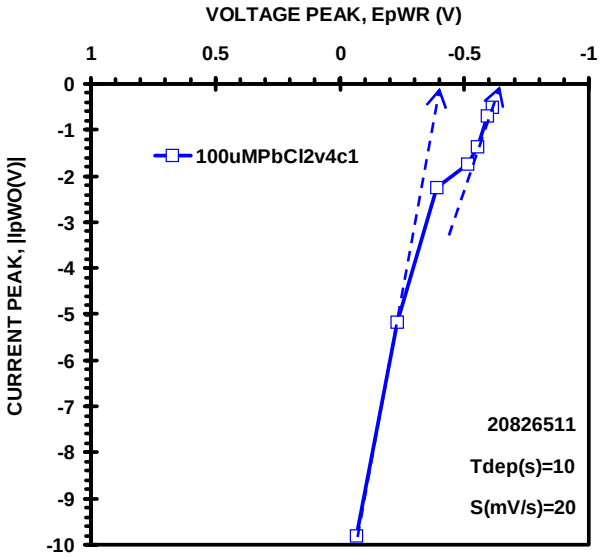

Figure 15c. ASV peak values derived from the 100 µM $PbCl_2$ data seen in Fig. 15a where $E_{p0}4$ = -0.35 V and $E_{p0}5$ = -0.60 V.

The ASV data are shown in Figs. 15a, 16a, 17a and 18a for seven Tdep times that range from 10 s to 1000 s in a 1, 2, 5 sequence. The voltage sweep rate wae 20 mV/s. This wave was generated using a step wave with 100 points. For a span of 2 V, each step is 20 mV with a duration of 1 s.

From an analysis of the D2ASV plot, the peak current-voltage was determined at each Tdep value and used to form the peak current-voltage curve. This curve is used to determine Ep_0 values by extrapolating the peak current-voltage curve to zero peak current. In order to determine the peak curve, the second derivative of the ASV data was calculated and shown in the D2ASV plots.

In the field of specroscopy [10], the second derivative of a function is used to identify the location of peaks and to identify shoulder peaks where two peaks are very close to each other. In this effort the second derivative of the ASV response was determined by fitting a second-order polynomial to the ASV data using a sliding five-point least-squares fitting method.

The second-order polynomial used to analyze the current, I, and voltage, V, curves is:

$$I = a_0 + a_1 \cdot V + a_2 \cdot V^2 \qquad (8)$$

where a_0, a_1, and a_2 are coefficients. The second derivitive is:

$$\frac{d^2 I}{dV^2} = 2a_0 \qquad (9)$$

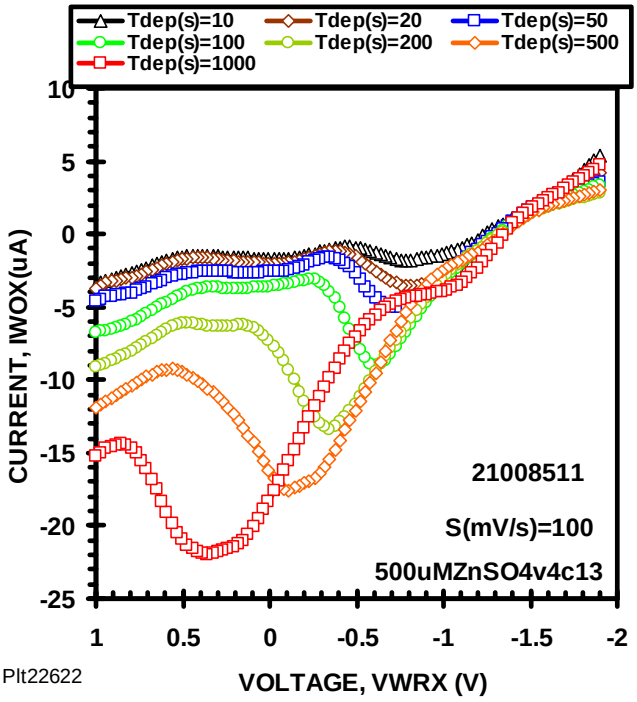

Figure 16a. ASV response for 500 µM $ZnSO_4$

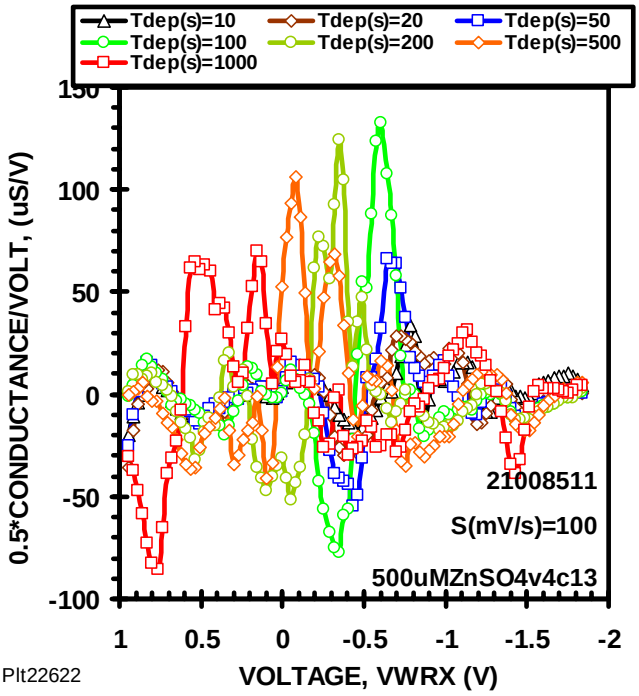

Figure 16b. D2ASV response for 500 µM $ZnSO_4$ data seen in Fig. 16a.

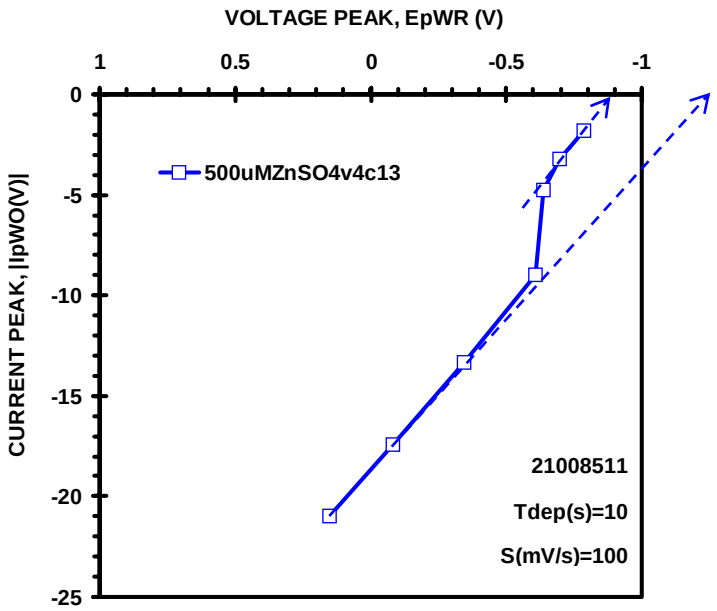

Figure 16c. ASV peak values derived from the 500 µM $ZnSO_4$ data seen in Fig. 16a where $E_{p0}6$ = -0.89 V and $E_{p0}7$ = -1.26 V.

The units of the second derivative are S/V. The coefficient a_0 is plotted in Figs. 15b, 16b, 17b and 18b. Notice that a_0 is 0.5 time the second derivative. The second derivative analysis was implemented in Excel using the LINEST function to fit the second-order polynomial in Eq. (8) to five adjacent points.

Concerning the second derivative (D2ASV) curves seen in Figs. 15b, 16b, 17b, and 18b, three observations are in order:

1. The base-line drift due to double-layer charging has been eliminated in the D2ASV curves..

2. The second derivative has a signficant negative going feature due to the lack of symmetry in the ASV response.

3. The second deriviative is a good method for identifying the location of peaks.

The method for determining peaks was automated. An Excel program was written that finds the peaks by sorting each of the D2ASV curves for the maximum peak value. A macro then copied the peak current and voltage for that Tdep curve to a new area in the Excel worksheet. Proceeding in this manner for each of the seven Tdep curves, an array of peak values was created. From this array, the peak value curves are charted and appear in Figs 15c, 16c, 17c and 18c. Then data in these curves were extrapolated to zero current, the intercept value.

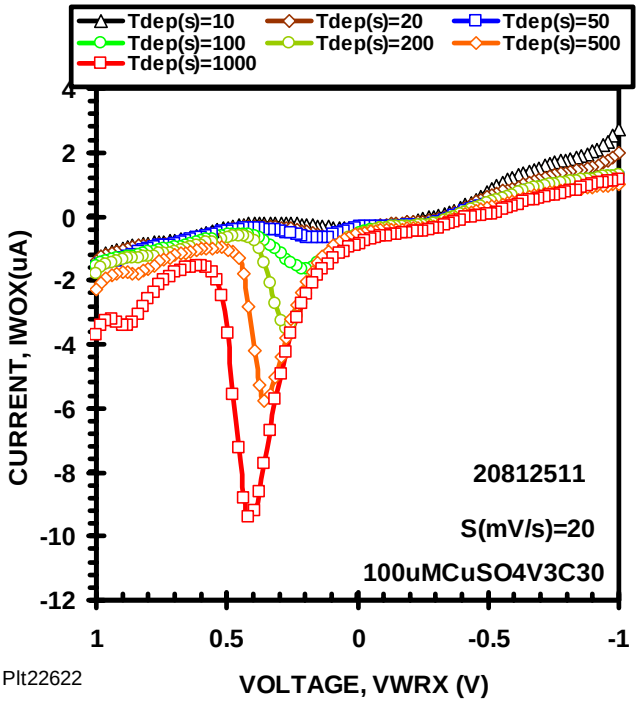

Figure 17a. ASV response for 100 µM $CuSO_4$

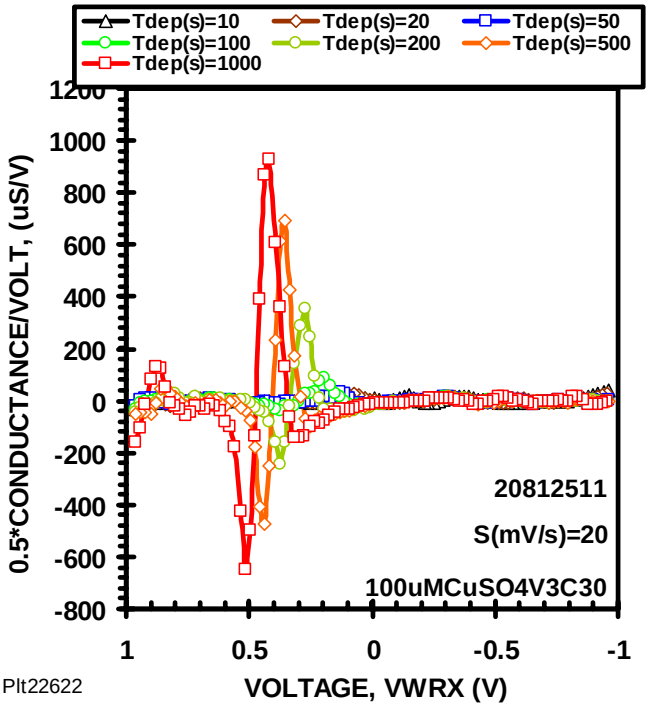

Figure 17b. D2ASV response for 100 uM $CuSO_4$ data seen in Fig. 17a.

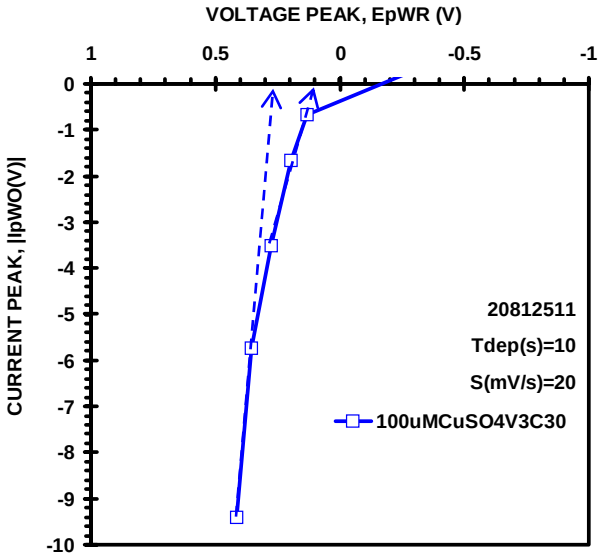

Figure 17c. ASV peak values derived from the 100 µM $CuSO_4$ data seen in Fig. 17a where $E_{p0}1$ = +0.28 and $E_{p0}2$ = +0.10 V.

The data clearly shows that two species are being oxidized as seen in Fig. 15, 16, and 17. This is most evident in the ASV curve seen in Fig. 15a for $PbCl_2$ and in the peak plot seen in Fig. 16c for $ZnSO_4$.

The results for the NaCl differ from the others. First, the peak current-voltage plot seen in Fig. 18c shows that the peak voltage does not vary with Tdep. This is suggestive of a totally reversible system. A possible explanation is that chlorine is reacting with the Ag in Pd(12)Ag(18) RE and forming AgCl. The voltage independence on Tdep suggests that it might be used as a calibrator ion when relating results to reduction potentials, E°, listed in the Electrochemical Series [6].

Another NaCl observation can be gleaned from the second derivative curves seen in Fig. 18b. They indicate that the ASV response curves seen in Fig. 18a are symmetrical. The symmetry of the NaCl ASV response is not shared by Pb, Zn, and Cu curves. Their second derivative curves are not symmetrical. These observations are key to understanding the nature of the interaction of the electroactive species with the WE.

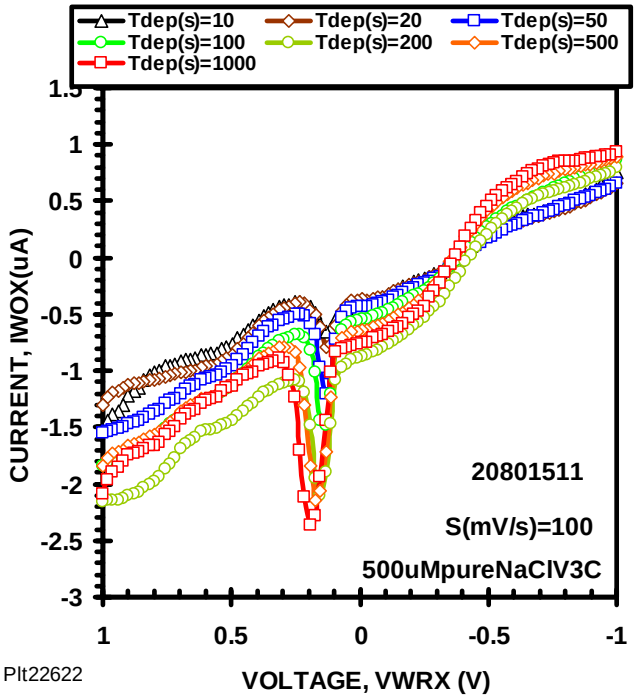

Figure 18a ASV response for 500 µM NaCl

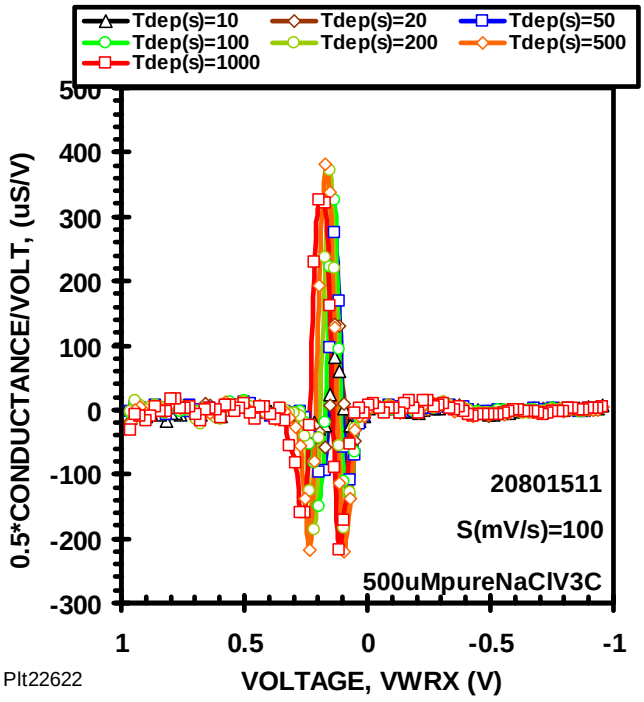

Figure 18b. D2ASV response for 500 uM NaCl data seen in Fig. 18a.

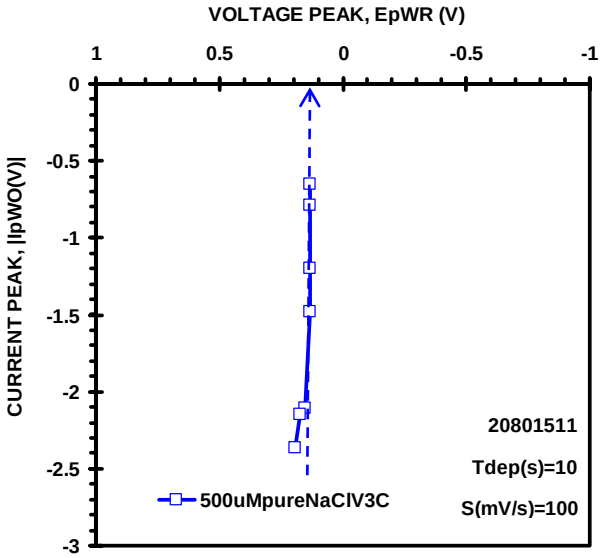

Figure 18c. ASV peak values derived from the 500 µM NaCl data seen in Fig. 18a where $E_{p0}3 = +0.133$ V.

9. ASV ANALYSIS

In this section the peak current-voltage curves seen in Figs 15c, 16c, 17c and 18c are analyzed for possible reactions. For the oxidation of a totally irreversible system, the ASV peak current-voltage relation is modeled [9] by:

$$I_p = -|I_{p0}|\exp[(1 - \alpha)\cdot f(E_p - E°)] \qquad (10)$$

where α is the transfer coefficient and $f = 38.92\ V^{-1}$ at 25°C. As seen in Figs 15c, 16c, 17c and 18c, the peak current-voltage relationship is linear. Linearizing Eq. 10, assuming the exponent is small, leads to:

$$I_p = -|I_{p0}|[1 + (1 - a)\cdot f(E_p - E_0)] \qquad (11)$$

where E_0 is the experimentally determined reduction potential. To determine E_0, I_p is set to zero in Eq. 11 which results in the following:

$$E_0 = E_{p0} + 1/[(1 - a)\cdot f] \qquad (12)$$

where E_{p0} is the $I_p = 0$ intercept value.

The possible reactions and their Reduction Potentials, E° are listed in Table 2. The E° values were corrected according to the ion concentration using the Nernst equation and are listed in the $E°_{corr}$ column. The E_{p0} values determind from Figs. 15 to 18 are listed in Table 2 along with E_0 values adjusted using Eq. 12 and $\alpha = 0.5$.

The $E°_{corr}$ and E_0 values are plotted in Fig. 19 and show a remarkable linear relationship. As shown in the inset to this figure, the least squares fit to this data indicates a slope of

1.26 and intercept of -0.1 V. Similar curves are reported elsewhere [1] and [11]. This cureve when well established will serve as as an aid in identifying ionic species.

Table 2. ASV Proposed Reactions and Potentials in Volts

Sym	Reaction	E°	$E°_{corr}$	E_{p0}	E_0
Cu2	$Cu^+ + e = Cu$	0.521	0.284	0.28	.331
Cu1	$Cu^{2+} + 2e = Cu$	0.342	0.224	0.133	.141
Ag	$Ag_2O + H_2O + 2e = 2Ag + 2OH^-$	0.342	0.244	0.09	.133
Pb2	$Pb^{2+} + 2e = Pb$	-0.126	-0.244	-0.4	-0.349
Pb1	$PbCl_2 + 2e = Pb + 2Cl^-$	-0.2675	-0.386	-0.65	-0.599
Zn2	$ZnOH^+ + H^+ + 2e = Zn + H_2O$	-0.497	-0.615	-0.9	-0.849
Zn1	$Zn^{2+} + 2e = Zn$	-0.762	-0.880	-1.25	-1.199

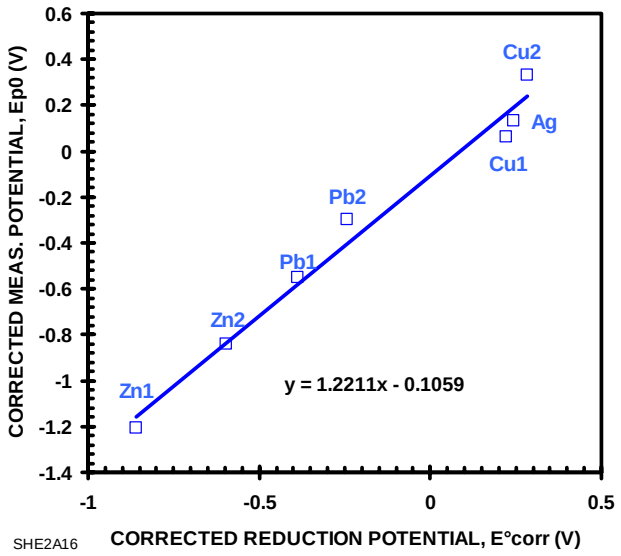

Figure 19. A reproducible linear relationship between the measured and standard reduction potentials may allow for identification of the ionic species.

10. WATER QUALITY

The next step in the development of water quality sensors is the development of repeatability and long-life sensors. The sensors are intended for use with the water reclamation system shown in Fig. 20. The system consists of gray water, which enters the bioreactor where a number of impurities are converted by the microbes within the bioreactor.

Biological nitrification [12] is a two-step process carried out by lithotrophic bacteria. Ammonia is oxidized to nitrite most commonly by bacteria of the genus Nitrosomonas by the following half-reaction:

$$NH_4^+ + 3/2\ O_2 = NO_2^- + 2H^+ + H_2O \qquad (13)$$

Nitrite is oxidized to nitrate by bacteria of the genus Nitrobacter by the half-reaction:

$$NO_2^- + 1/2\ O_2 =. NO_3^- \qquad (14)$$

The sensor locations are indicated in Fig. 20. The sensors need to have adequate sensitivity and lifetime when exposed to various inorganics, organics, and biofilms. Sensors will be inserted in the inlet line where they are exposed to gray water, in the bioreactor where they are exposed directly to biofilms, and in the outlet line where they are exposed to potable water. At the outlet, the sensors need to have high sensitivity in order to detect residual contaminants.

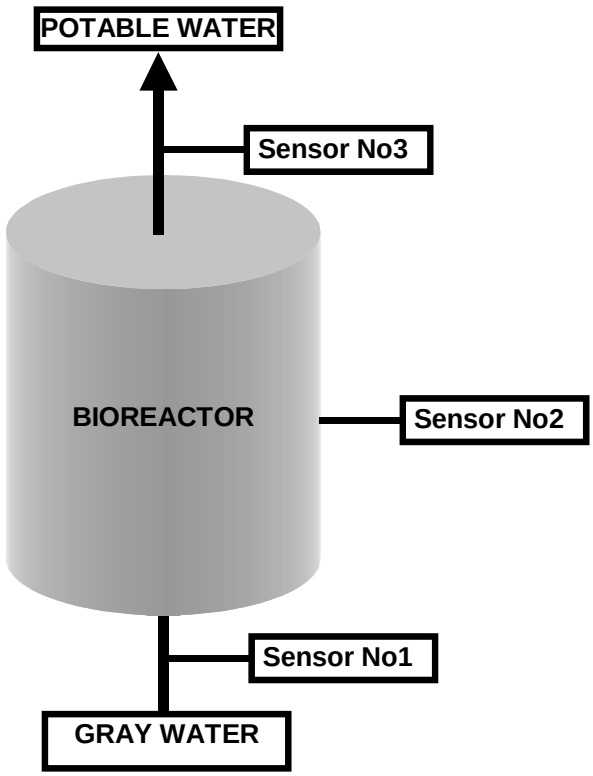

Figure 20. Bioreactor system with sensors located to monitor the functioning of the bioreactor system.

An approach to long-life electrochemical sensors uses the four cleaning and preservation methods depicted in Fig. 21 to maintain the surface of the electrochemical sensors in a state so that they provide data on the functioning of the bioreactor. Mechanical wiping is one approach but it is recognized that this approach could have limited applicability due to the build-up of biofilms on the wipers and scratching of sensitive films covering Ion Selective Electrodes. A study is needed to determine which of the

techniques shown in Fig. 21 will be effective in providing accurate, long-life sensors.

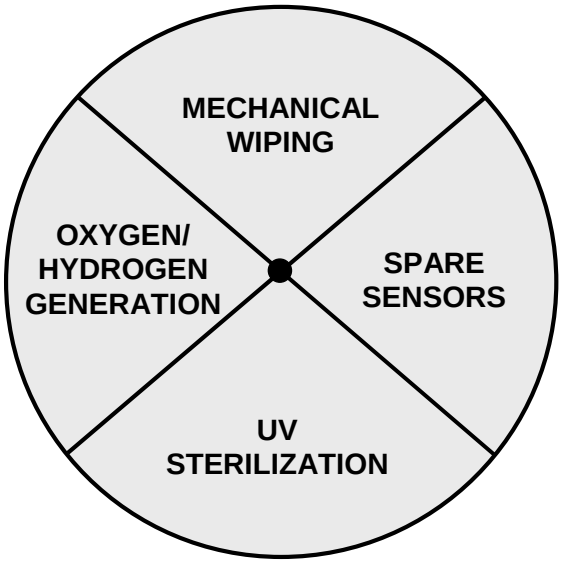

Figure 21. Cleaning and preservation methods for long-life bioreactor sensors. Sensor wiping effort is already funded on another effort. The other methods are the focus of this effort.

11. DISCUSSION

The knowledge gained on this effort has provided key insights into the fabrication and instrumentation of planar bare metal sensors. Use of the planar configuration opens up as number of application areas such as cleaning using wiping techniques and see-through chambers where the electrodes are fabricated opposite optically transparent windows. The ability to array the REDOX sensors with a common ground is critical in developing much larger sensor arrays. Understanding the conductivity sensor circuitry is critical in eliminating between sensors. In these studies, it was discovered that to eliminate interference between sensor, unused sensors must be turned off by setting the sensor current to zero. This requires that the sensor be configured as a galvanostat not a potentiostat.

The material choices for the electrodes have led us away from the use of bare Ag RE because of the Ag dendritic growth characteristics. In subsequent designs the Ag will be replaced with other materials.

Finally, the analytical procedures developed on this effort are keys to identifying the nature of the electroactive species. The technique of extrapolating the ASV peak current and voltage curves to zero current where E_0 can be identified could be an important new development in facilitating identifying the nature of the electroactive species. This understanding gained on this effort provides the basis for the next phase in developing long-life water quality sensors.

12. ACKNOWLEDGMENTS

The work described in this paper was performed by the Jet Propulsion Laboratory, California Institute of Technology, under a contract with the National Aeronautics and Space Administration. The overall effort is supported by a grant from the National Aeronautics and Space Administration under the Advanced Environmental Monitoring and Control Program. The authors are indebted to our program manager, Darrell Jan, for his support. In addition, we are pleased to acknowledge the efforts of Dennis Martin and Kent Fung, Halcyon Microelectronics, Inc. Irwindale, CA in the fabrication of E-Tongue 2. File: AeroRedox2C14.doc.

13. REFERENCES

[1] M. G. Buehler, G. M. Kuhlman, D. Keymeulen, and S. Kounaves, "Advanced Electronic Tongue Concept", *2002 IEEE Aerospace Conference*, 2002, *Vol. 1, cat. No.* 02TH8593C.

[2] P. T. Kissinger and W. R. Heineman, *Laboratory Techniques in Electroanalytical Chemical*, Marcel Dekker (New York, 1996).

[3] J. Wang, *Analytical Electrochemistry*, Wiley-VCH, New York, 2000.

[4] S. J. West, X. Wen, R. Geis, J. Herdan, T. Gillette, M. H. Hecht, W. Schubert, S. Grannan, S. P. Kounaves, "Electrochemistry on Mars," American Laboratory 31 (20), p. 48–, Oct. 1999.

[5] "Methods for Developing Spacecraft Water Exposure Guidelines", The National Academy of Sciences, 2000 (Page 126, Table A2).

[6] Handbook of Chemistry and Physics, Electrochemical Series, No. 74, CRC Press (Boca Raton, 1994).

[7] R. Feeney, J. Herdan, M. A. Nolan, S. H. Tan, V. Tarasov, and S. P. Kounaves, "Analytical Characterization of Microlithographically Fabricated Iridium-Based Ultramicroelectrode Arrays", Electroanalysis, 1998, 10, No.2, 89-93.

[8] M. G. Buehler and W. R. Thurber, "A Planar Four-Probe Test Structure for Measuring Bulk Resistivity," IEEE Trans. On Electron Devices, Vol. ED-23, pp. 968-974.1976.

[9] A. J. Bard and L. R. Faulkner, *Electrochemical Methods*, 2nd Edition, Wiley & Sons (New York, 2001).

[10] D. Diamond and V. C. A. Hanratty, *Spreadsheet Applications in Chemistry using Microsoft Excel*, J. Wiley & Sons (New York, 1997).

[11] G.T.A. Kovacs, C. W. Storment and S. P. Kounaves, Sensors and Actuators B, 23, 41-47, 1995.

[12] Y. Sakano, K. D. Pickering, P. F. Strom, and L. J. Kerkhof, "Spatial Distribution of Total, Ammonia-Oxidizing, and Denitrifying Bacteria in Biological Wastewater Treatment Reactors for Bioregenerative Life Support", Applied And Environmental Microbiology, May 2002, p. 2285–2293 Vol. 68, No. 5.